

High strength-ductility Co₂₃Cr₂₃Ni₂₃Mn₃₁ medium-entropy alloy achieved via defect engineering

Jianying Wang¹, Hailin Yang^{1,*}, Hua Huang¹, Jianpeng Zou¹, Shouxun Ji², Zhilin Liu^{3,*}

1. State Key Laboratory of Powder Metallurgy, Central South University, Changsha 410083, P.R. China

2. BCAST, Brunel University London, Uxbridge, Middlesex, UB8 3PH, United Kingdom

3. Light Alloy Research Institute, College of Mechanical and Electrical Engineering, Central South University, Changsha, 410083, P.R. China

* Corresponding authors: y-hailin@csu.edu.cn; zhilin.liu@csu.edu.cn

Abstract:

We employed ‘defect engineering’ to achieve high strength-ductility in a new Co₂₃Cr₂₃Ni₂₃Mn₃₁ medium-entropy alloy. Yield strength, ultimate tensile strength and fracture strain reached 1.18 GPa, 1.71 GPa and 65.2% at cryogenic temperature, respectively. Mechanical improvement resulted from synergy of nanoparticles, dislocations, stacking faults, nanotwins, Lomer-Cottrell locks, h.c.p lamellae and amorphous bands.

Keywords: Medium-entropy alloys; Microstructural defects; Tensile properties; Deformation structure; Strengthening mechanisms

1. Introduction

Medium-entropy alloys (MEAs), an alloy design strategy similar to high-entropy alloys (HEAs), consist of two to four elements in equiatomic or near-equiatomic constituents. They have drawn much attention in research communities due to their attractive mechanical response [1-4]. Compared with conventional alloys, their superior properties do not result from a single dominant component, such as iron in steel, nickel in superalloy and WC in cemented carbide, but rather entropically stabilized from the synergistic effects of multiple elements with the potential for unique combinations of mechanical properties [4-6].

Recently, intensive studies have shown that the lattice defects significantly contributed to strengthening and toughening of MEAs [7-11]. Besides very low stacking fault energy, the MEAs usually present face-centred cubic (f.c.c) and/or hexagonal-close packed (h.c.p) lattice structures. Thus, the most commonly observed lattice defects, i.e. dislocations, stacking faults (SFs), Lomer-Cottrell locks (LCs), nanotwins, and phase transition, tend to form readily during materials processing or tensile deformation [8-10]. The superior strength-ductility in these alloys with such lattice defects is resulted from the strain hardening capacity initiated by individual or multiple strengthening mechanisms. For instance, the CoCrFeNi alloy can facilitate formation of nanotwin boundaries and blockage of dislocation glide during straining, which delivered the excellent strength / elongation 1.2 GPa / 13.6% [9]. Meanwhile, the transformation-induced plasticity (TRIP) effect, along with enhanced mechanical properties, was frequently reported in the high-Mn MEA systems [11-13]. Compared with its perfect single-phase counterpart, an appropriate combination of defects led to better strength-ductility synergy in the Fe₅₀Mn₃₀Co₁₀Cr₁₀ alloy [11].

Moreover, previous studies have shown that HEAs/MEAs containing Cr, Mn, Fe, and Co atoms exhibit strong temperature dependence of SF energy [14, 15]. The cryogenic temperature corresponds to the small SF energy. Further, the small SF energy promotes extensive activities of Shockley partial dislocations and the formation of higher density defects (i.e. SFs, shear bands and nanotwins). Plastic deformation can be dominated by motion of Shockley partial dislocations and full dislocations, deformation twinning, and even f.c.c → h.c.p phase transformation at lower temperatures [16-20]. The CrMnFeCoNi and Fe₆₀Co₁₅Ni₁₅Cr₁₀ MEAs with single f.c.c phase showed superior ductility (70% and 87%) and high strength (0.76 GPa and 1.5 GPa) at low temperature of 77 K, respectively [14, 19, 20].

In the present work, we intentionally introduced lattice defects into a newly-developed Co₂₃Cr₂₃Ni₂₃Mn₃₁ medium-entropy alloy through thermomechanical process. Then, the tensile deformation behaviour at various strain levels was examined at room and cryogenic temperatures, respectively. The new Co₂₃Cr₂₃Ni₂₃Mn₃₁ medium-entropy alloy exhibited high strength-ductility, in

particular at cryogenic scenario. Experimental results indicate that the formation of defects, including nanoparticles, LCs, nanotwins, f.c.c \rightarrow h.c.p phase transition, and amorphous bands, contributed to strengthening and toughening the as-deformed $\text{Co}_{23}\text{Cr}_{23}\text{Ni}_{23}\text{Mn}_{31}$ medium-entropy alloy.

2. Experimental

The as-cast $\text{Co}_{23}\text{Cr}_{23}\text{Ni}_{23}\text{Mn}_{31}$ (at.%) alloy was produced by melting pure Co, Cr, Ni and Mn metals (> 99.8 wt.% purity) in a vacuum induction furnace. The as-cast cubic ingot ($10 \times 30 \times 60$ mm³) was rolled by 50% in thickness at 1173 K. Subsequently, the 5 mm-thick alloy sheets were homogenized at 1373 K for 2 h in Ar atmosphere, followed by water quenching. To obtain samples with fine grain sizes, the homogenized alloy was further cold-rolled from 5 to 2.5 mm in thickness at 298 K. Then, the cold-rolled samples were annealed at 1173 K in Ar atmosphere for 30 min before water quenching. Dog-bone-shaped tensile samples with a gauge length of 30 mm and cross-section of 2.2×1.5 mm² were prepared by electrical discharge machining. Both sides of the samples were carefully ground to a 2000 grit finish using a SiC paper. The uniaxial tensile tests were performed using a material testing system (MTS Alliance RT30) tension machine at strain rate of 1×10^{-3} s⁻¹.

Phase constituents of the samples were identified by X-ray diffraction (XRD, Rigaku X-2000) at 40 kV with Cu K_{α} radiation ($\lambda_{\text{ka}} = 1.54$ Å). Microstructure features of the alloys were analyzed using multiple techniques. Electron backscatter diffraction (EBSD) measurements were carried out in a FIB Helios NanoLab G3 UC scanning electron microscope (SEM). EBSD is equipped with a Hikari camera and the TSL OIM data analysis software. To distinguish the deformation mechanisms of alloys, microstructural characterization was further conducted using transmission electron microscopy (TEM; Tecnai G2 F20). TEM specimens were prepared using the mechanical polishing and the precision ion polishing system (PIPS) at a voltage of 5 kV and an incident angle of $3 \sim 7^{\circ}$.

3. Results and discussion

SEM and EBSD images for the microstructure of as-cast $\text{Co}_{23}\text{Cr}_{23}\text{Ni}_{23}\text{Mn}_{31}$ alloy are shown in Fig. 1(a) and (b), respectively. Many macroscale annealing twins (~ 100 μm) were observed. The average grain sizes of f.c.c phase were 33.75 μm . There is no pronounced texture, as shown by the Inverse pole figure in Fig. 1(b). XRD patterns in Fig. 1(c) verified that the alloy consists of only f.c.c crystal structure. In addition, the EDS chemical mapping in Fig. 1(d) confirmed uniform distribution of individual Co, Cr, Ni and Mn atoms. Fig. 2(a) shows the pseudo 3D microstructure of as-deformed $\text{Co}_{23}\text{Cr}_{23}\text{Ni}_{23}\text{Mn}_{31}$ alloy, having full equiaxed or near-equiaxed grains with an average size of 13.12 μm . Some typical deformation twins were also determined, as verified by the 60° misorientations in Fig. 2(b). EBSD phase mapping and IPF image in Fig. 2(c) and (d) confirmed

the transformation from f.c.c to h.c.p phases in the as-deformed samples. This EBSD result in Fig. 2(c) agrees well with the XRD spectra in Fig. 1(c).

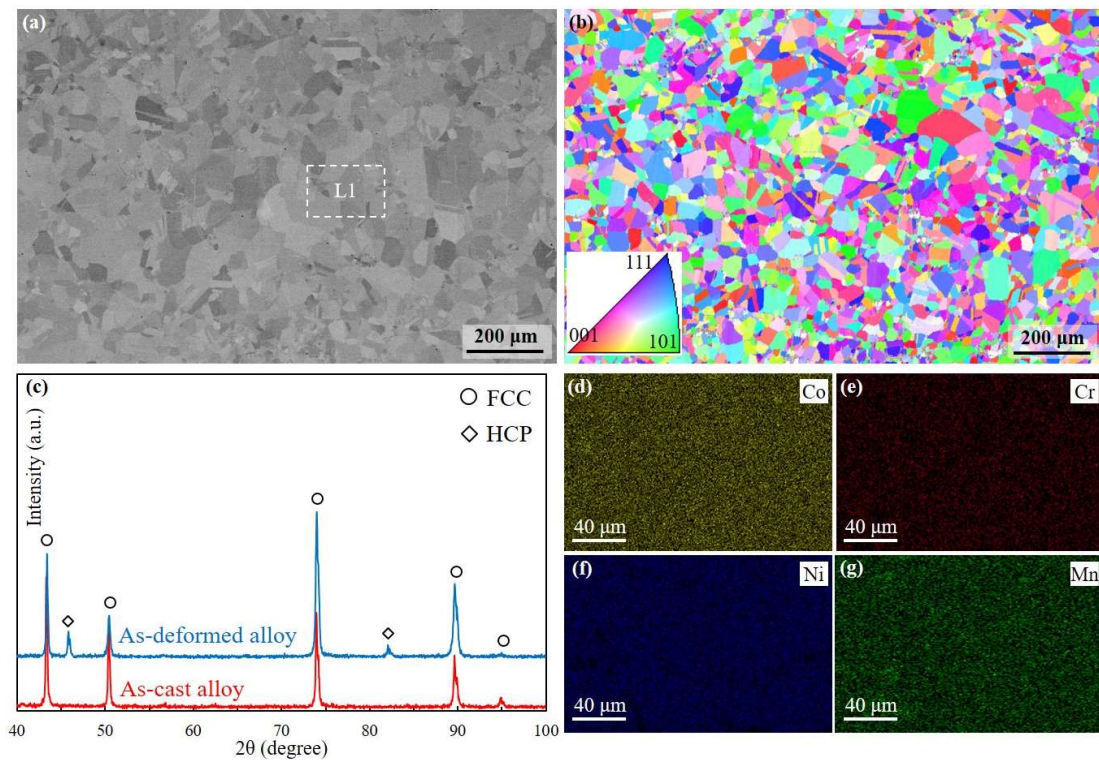


Fig. 1. (a) SEM and (b) EBSD orientation mapping images, showing the microstructural features of as-cast $\text{Co}_{23}\text{Cr}_{23}\text{Ni}_{23}\text{Mn}_{31}$ alloy; (c) XRD spectra of the as-cast and as-deformed $\text{Co}_{23}\text{Cr}_{23}\text{Ni}_{23}\text{Mn}_{31}$ alloy; (d) – (g) EDS elemental mapping of the L1 area in (a), indicating uniform distribution of Co, Cr, Ni and Mn, respectively.

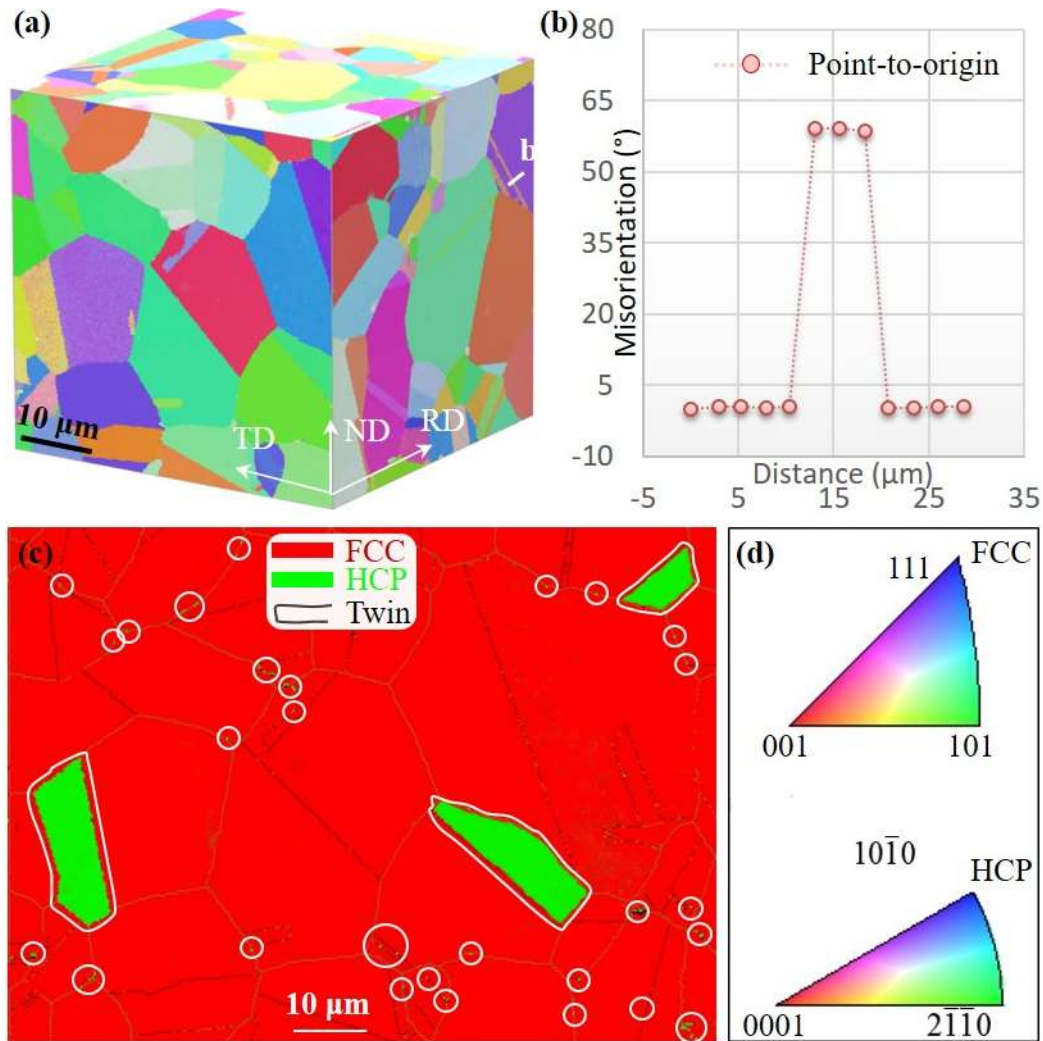


Fig. 2. The pseudo three-dimensional (3D) EBSD orientation mapping image, displaying grain structures of as-deformed $\text{Co}_{23}\text{Cr}_{23}\text{Ni}_{23}\text{Mn}_{31}$ alloy; (b) Misorientation degrees along the white line **b** in (a), identifying representative deformation twins; (c) EBSD phase mapping image of the as-deformed alloy, showing f.c.c \rightarrow h.c.p phase transformation; and (d) Inverse pole figures of the f.c.c and h.c.p phases in (c). The white circle areas in (c) indicate very small newly-formed h.c.p phase particles (Readers can enlarge picture for details).

The uniaxial stress-strain curves collected from tensile tests are shown in Fig. 3(a). The yield strength (YS), ultimate tensile strength (UTS) and fracture strain of as-cast alloy tested at 298 K are 0.40 GPa, 0.57 GPa and 64.4%, respectively. Combination of cold rolling and annealing significantly enhanced the tensile strength, but with certain sacrifice of ductility. The YS, UTS and fracture strain values of $\text{Co}_{23}\text{Cr}_{23}\text{Ni}_{23}\text{Mn}_{31}$ alloy tested at 298 K are 0.74 GPa, 1.26 GPa and 43.9%, respectively. When decreasing the testing temperature to 77 K, the YS and UTS values of as-deformed alloy were increased to 1.18 GPa and 1.71 GPa, respectively. Meanwhile, the fracture strain reached a maximum value of 65.4%. Fig. 3(b) shows a comparison of the tensile properties of $\text{Co}_{23}\text{Cr}_{23}\text{Ni}_{23}\text{Mn}_{31}$ alloy under different conditions with various advanced steels, traditional alloys, and other MEAs and HEAs with superior mechanical properties [17-24]. The newly-developed $\text{Co}_{23}\text{Cr}_{23}\text{Ni}_{23}\text{Mn}_{31}$ alloy in the present work shows a remarkable tensile strength-ductility synergy,

in particular better than the previously reported precipitation-hardened HEAs, metastable brittle HEAs, carbon-doped HEAs, and dual-phase HEAs [21-24]. The fractured surface in Fig. 4(a) shows that the extremely high fracture toughness of as-deformed alloy tested at 77 K. Numerous microvoid coalescence occurred on the fracture surface. Nearly, every microvoid has embedded with one nanoparticle inside. The large number of nanoparticles were determined as the Cr oxides, as indicated by the EDS chemical mapping in Fig. 4(b) – (g). However, there are only minor such nanoparticles present in the as-cast tensile samples (see Supplementary Fig. S1). These nanoparticles mainly formed during annealing treatment. Additionally, trace analysis of tensile samples suggests that the plastic deformation in $\text{Co}_{23}\text{Cr}_{23}\text{Ni}_{23}\text{Mn}_{31}$ resulted from the high-density of dislocation walls (HDDWs). HDDWs traces were highlighted by the yellow arrows in Fig. 4(a).

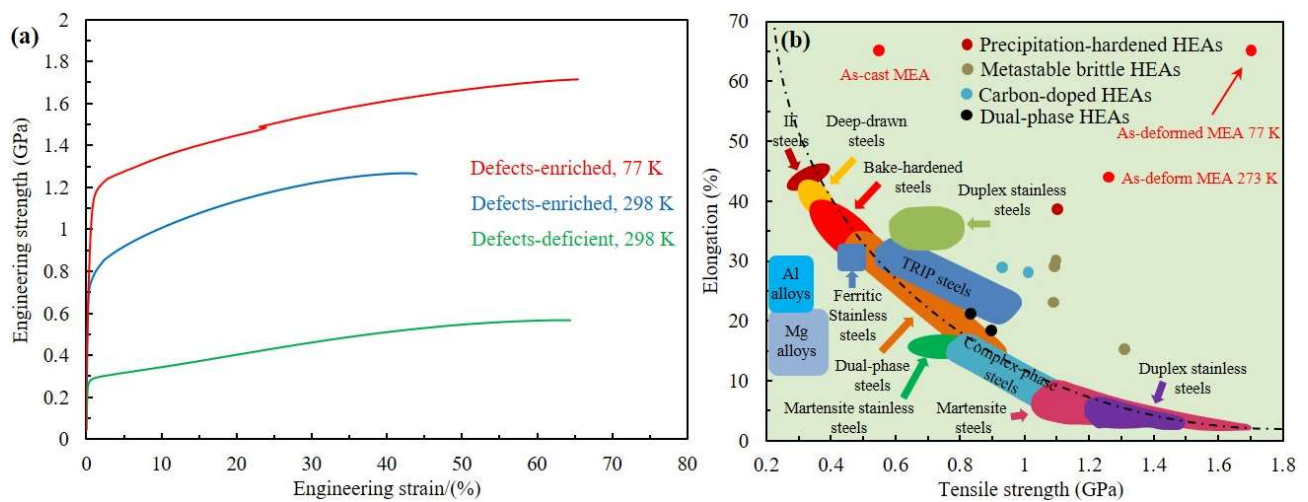


Fig. 3. (a) Engineering stress – strain curves of the $\text{Co}_{23}\text{Cr}_{23}\text{Ni}_{23}\text{Mn}_{31}$ alloy tensile samples, tested under different conditions; (b) Comparison of the tensile properties between the $\text{Co}_{23}\text{Cr}_{23}\text{Ni}_{23}\text{Mn}_{31}$ alloy, Al alloys, Mg alloys, steels, and high-entropy alloys [32-35].

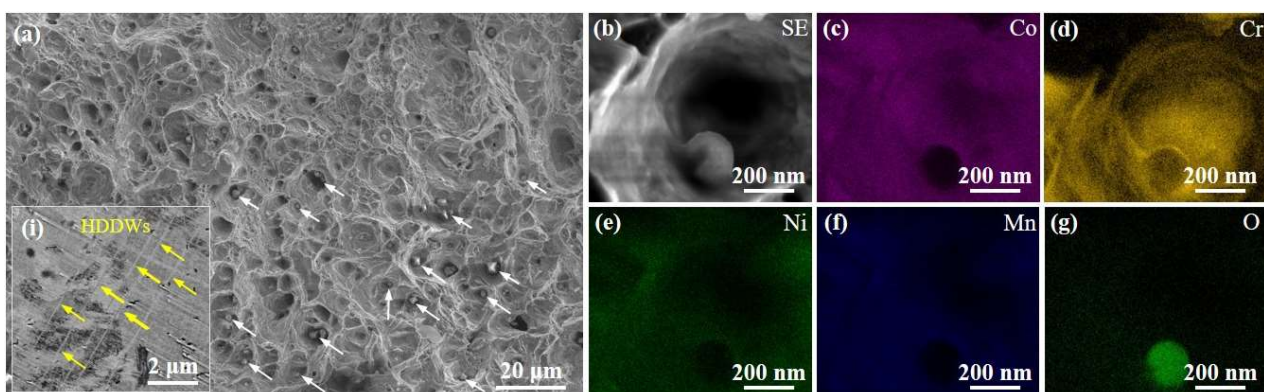


Fig. 4. (a) SEM micrograph of the as-deformed $\text{Co}_{23}\text{Cr}_{23}\text{Ni}_{23}\text{Mn}_{31}$ alloy tensile samples at 77 K, showing fully ductile fracture; (b) SEM image of one nanoparticle sitting inside a microvoid, collected randomly from (a); (c) – (g) EDS chemical mapping of the nanoparticle in (b). The white and yellow arrows in (a) highlight the existence of some nanoparticles and the high-density of dislocation walls (HDDWs), respectively.

Further, the detailed TEM investigation was conducted on the as-deformed tensile samples for different strain levels. At a low strain value of 10%, the deformation strengthening is dominated by the higher-density mobile dislocations and the Orowan's effect (i.e. dislocations-nanoparticles interactions), as shown in Fig. 5(a). The bright field (BF) and high-resolution TEM (HRTEM) images in Fig. 5(b) and (c) display high-density SFs within the f.c.c parent matrix, revealing that the $\text{Co}_{23}\text{Cr}_{23}\text{Fe}_{23}\text{Ni}_{31}$ alloy has very low SF energy. It would promote to generate profuse partial dislocations in such case. SAED pattern along the $[011]_{\text{f.c.c}}$ zone axis in Fig. 5(c) identifies a monolayer of SFs on (111) and $(11\bar{1})$ planes. Intersections of these SFs led to formation of Lomer-Cottrell locks (LCs). The LCs-driven strengthening and hardening originates from their capability to accommodate dislocations. Normally, four dislocation segments are pinned by each LC lock with short length. Every LC lock could equivalently act as a pinning point (or pinning particle), similar to Orowan's effect [25-27]. Thus, the interactions between the high density mobile dislocations and the nanoparticles / LCs caused the high YS value of $\text{Co}_{23}\text{Cr}_{23}\text{Fe}_{23}\text{Ni}_{31}$ alloy deformed at 77 K. As the engineering strain increased to 34%, the formation of multiple nanotwins (~ several tens of nanometres) and their intersections became predominant in Fig. 5(d). The twin-twin intersections, as well as twin boundary migration, could accommodate numerous dislocations to sustain plastic deformation of f.c.c metals [28, 29]. This case is particularly operated for extreme deformation at low temperatures [28-31].

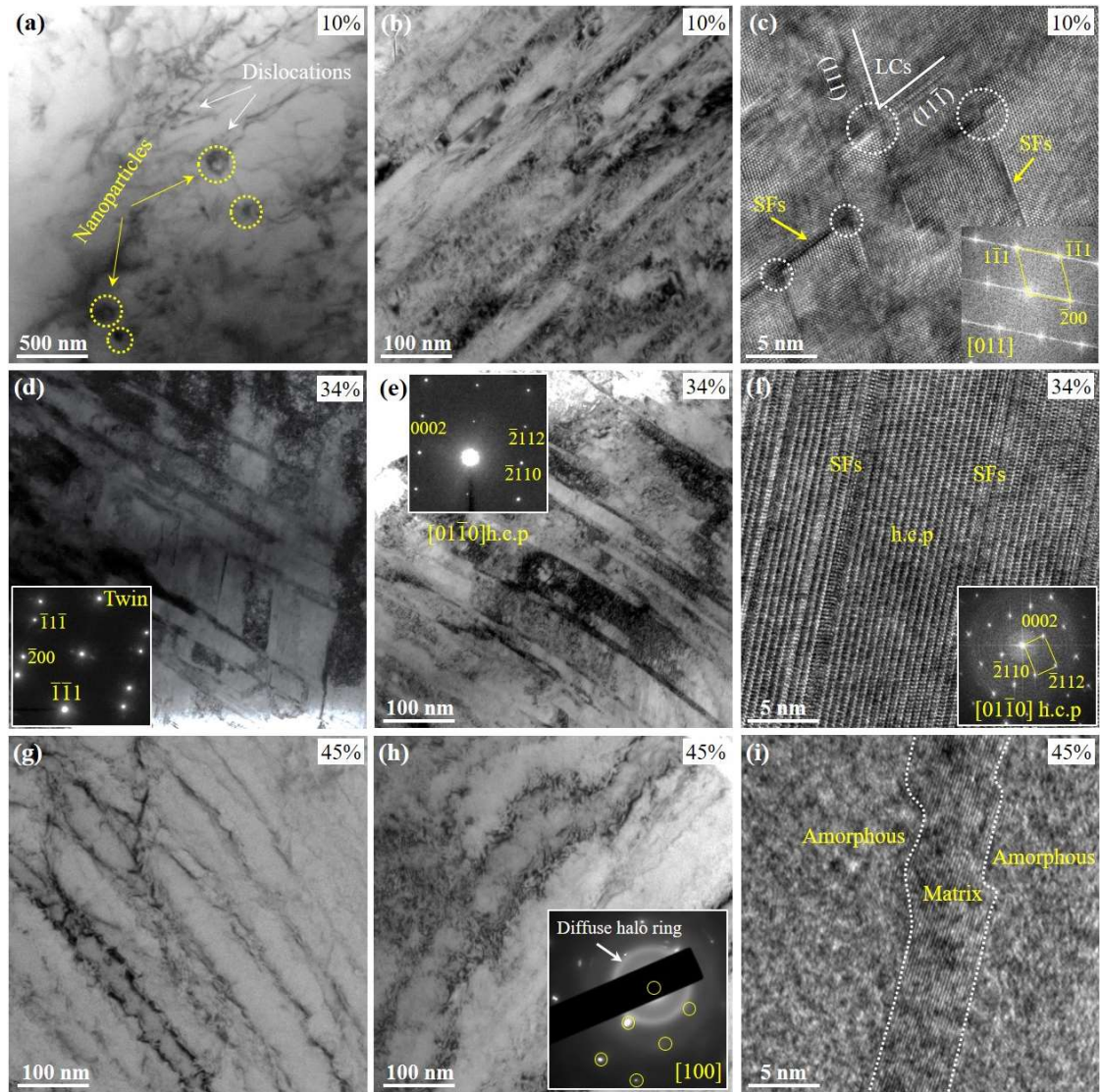


Fig. 5. Microstructural evolution of the as-deformed $\text{Co}_{23}\text{Cr}_{23}\text{Ni}_{23}\text{Mn}_{31}$ alloy at 77 K with different strain levels, including (a) – (c) 10%, (d) – (f) 34%, and (g) – (i) 45% strain. (a) the interactions between nanoparticles and dislocations at strain of 10%; (b) bright-field TEM and (c) high-resolution TEM images at strain of 10%, showing the formation of stacking faults (SFs) and Lomer-Cottrell locks (LCs); (d) the interactions of multiple nanotwins at strain of 34%; (e) bright-field TEM and (f) high-resolution TEM images at strain of 34%, showing the formation of new h.c.p phase lamellae; (g) bright-field TEM image and (h) electron diffraction patterns at strain of 45%, showing the formation of amorphous bands; and (i) high-resolution TEM image, showing the interfaces between amorphous bands and crystalline matrix.

Meanwhile, the intersections between multiple nanotwins within each individual grain will generate new interfaces, dislocation jogs, and dislocation kinks [31-34]. These newly-formed interfaces, in turn, will block or hinder mobile dislocations [31], which further contributes to strengthening. With increasing engineering strain to 34%, the h.c.p lamellae were observed in the microstructure (Fig. 5(e)). It has been reported that nanoscale SFs can function as the nuclei of h.c.p lamellae [35]. Nucleation and glide of Shockley partial dislocations enable to correct SFs, which promotes the high density SF regions transform into the h.c.p structure [35]. The HRTEM image in Fig. 5(f) shows the residual SFs inside the newly-formed h.c.p lamellae. In the present work, the

SF regions developed into the h.c.p lamellae at large strain value of 34%. Moreover, the transformation (f.c.c \rightarrow SFs \rightarrow h.c.p) in $\text{Co}_{23}\text{Cr}_{23}\text{Ni}_{23}\text{Mn}_{31}$ alloy continuously engendered new SF/h.c.p. interfaces, which reduced the average free path for dislocations. Again, mobile dislocations were blocked and piled up around the new interfaces. Taken together, these factors (i.e. the high density SFs, nanotwins, and the h.c.p lamellae) at 77 K synergistically generated massive interface defects. Further, these defects engineered by thermomechanical process dramatically improved the strengthening and/or hardening capacity. Thus, the strength-ductility synergy was achieved in the $\text{Co}_{23}\text{Cr}_{23}\text{Ni}_{23}\text{Mn}_{31}$ alloy, as is reported elsewhere [8, 36].

Besides the nanoscale SFs, LCs, nanotwins and h.c.p lamellae, some amorphous bands were also detected, as shown in Fig. 5(g) and (h). The bright-field TEM images in Fig. 5(g) and (h) were taken along the $[100]_{\text{f.c.c}}$ zone axis. When the engineering strain reached 45%, the amorphous bands occurred in the f.c.c $\text{Co}_{23}\text{Cr}_{23}\text{Ni}_{23}\text{Mn}_{31}$ alloy matrix. The thickness of these amorphous bands was measured to be 20 ~ 70 nm. The high-resolution TEM image in Fig. 5(i) demonstrates the clear and sharp interfaces between amorphous bands and f.c.c matrix. Like the interfaces introduced by nanotwins and h.c.p lamellae, the amorphous/matrix interfaces could also favourably accommodate high density dislocations and simultaneously hinder dislocation movements [37, 38]. Actually, the amorphous bands deliver even higher thermal stability than the nanotwins and h.c.p lamellae. Using tempering treatment at relatively higher temperatures, the amorphous bands enable to increase strain hardening capacity, but without sacrificing the YS values [36]. Microstructural characterization of the $\text{Co}_{23}\text{Cr}_{23}\text{Ni}_{23}\text{Mn}_{31}$ alloy deformed at 298 K is shown in Fig. 6. At low strain value of 10%, dislocation strengthening was identified as dominant mechanism responsible for mechanical improvement (Fig. 6(a)). At medium strain value of 20%, the dislocations, together with high density SFs and LCs, drove plastic flow at high strain hardening. The dislocations and high density SF and LCs were confirmed in Fig. 6(b) – (d). However, twins and dislocations were determined as the major microstructural feature at high strain (32%), as shown in Fig. 6(e) and (f). Deformation twinning and mobile dislocations become primary deformation mechanisms in such case.

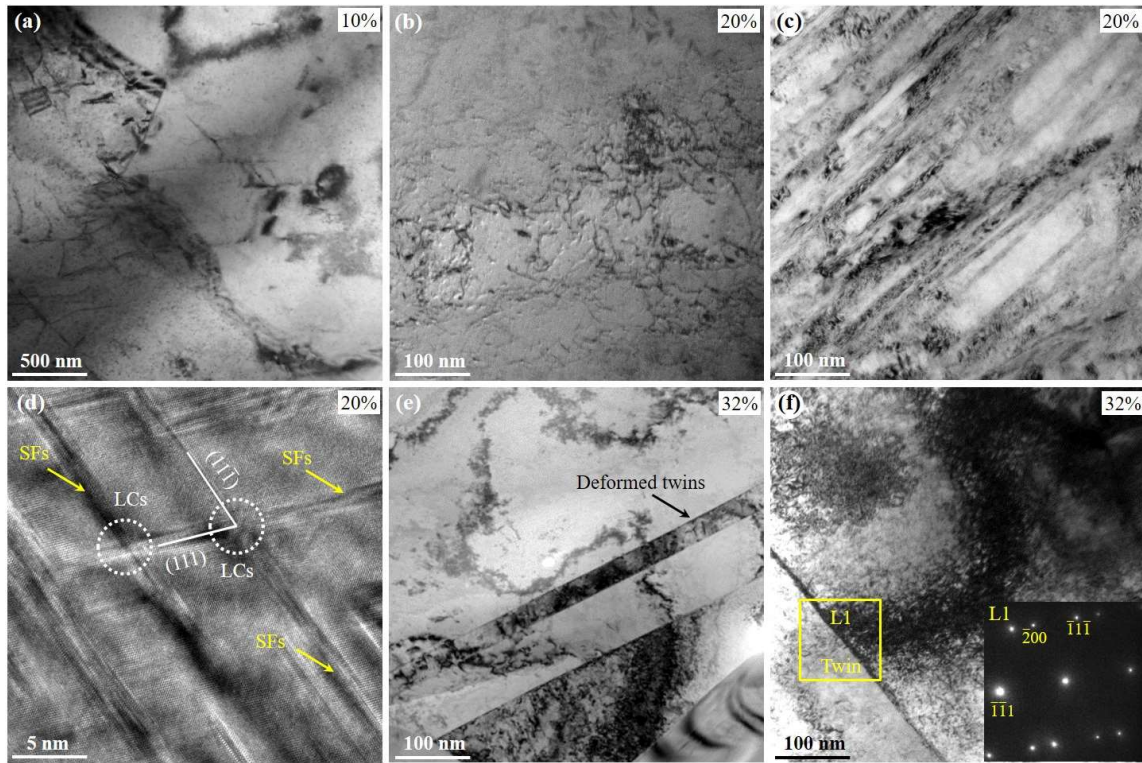


Fig. 6. Dynamic evolution of the deformation substructures of the as-deformed $\text{Co}_{23}\text{Cr}_{23}\text{Ni}_{23}\text{Mn}_{31}$ alloy at 298 K with different strain levels, including (a) 10%, (b) – (d) 20%, and (e) – (f) 32% strain. (a) Formation of dislocations at strain of 10%; (b) Formation of dislocations at strain of 20%; (c) Bright-field and (d) high-resolution TEM images, showing formation of high density SFs and LCs; and (e) Formation of deformation twins and (f) interaction between twin boundaries and mobile dislocations. Diffraction pattern in (f) was collected from the yellow square area in (f), confirming deformation twins.

4. Conclusions

In summary, a large quantity of different defects (i.e. nanoparticles, dislocations, deformation twins, stacking faults, Lomer-Cottrell locks (LCs), h.c.p. bands, and amorphous bands) were engineered in the $\text{Co}_{23}\text{Cr}_{23}\text{Ni}_{23}\text{Mn}_{31}$ medium-entropy alloy by thermomechanical process. Compared with the as-cast single f.c.c phase counterpart having deficient defects, the defects-enriched $\text{Co}_{23}\text{Cr}_{23}\text{Ni}_{23}\text{Mn}_{31}$ alloy exhibited superior mechanical properties at room and cryogenic temperatures. At 298 K, the defects-enriched alloy showed yield strength of 0.74 GPa and fracture strain of 43.9%. Moreover, the yield strength and fracture strain are increased to 1.18 GPa and 65.2% at 77 K, respectively. These tensile properties are otherwise inaccessible for their defects-deficient counterparts (0.26 GPa and 64.07%) at 298 K. The enhanced mechanical properties are mainly attributed to the interactions of LCs and/or nanoparticles with mobile dislocations, similar to Orowan's strengthening mechanism. Meanwhile, numerous nanostructures (i.e. nanotwins, h.c.p lamellae and amorphous bands) formed during tensile deformation at different strain levels. These nanostructures simultaneously supervene with generating massive new interfaces with their surrounding f.c.c matrix. Further, these nanostructures and new interfaces not only accommodate

plastic flow, but also serve as strong barriers for mobile dislocations, resulting in materials strengthening and toughening.

Declaration of competing Interest

The authors declare that they have no known competing financial interests or personal relationships that could have appeared to influence the work reported in this paper.

CRedit authorship contribution statement

Jiaying Wang: Data curation, Writing - original draft, Investigation. **Hailin Yang:** Conceptualization, Funding acquisition, Project administration, Writing - review & editing, Supervision. **Hua Huang:** Investigation. **Jianpeng Zou:** Investigation. **Shouxun Ji:** Writing - review, Investigation. **Zhilin Liu:** Conceptualization, Project administration, Writing - review & editing, Supervision.

Acknowledgments

This project was financially supported by National Natural Science Foundation of China with No. 51404302.

References

- [1] E.W. Huang, D.J. Yu, J.W. Yeh, C. Lee, K. An, A study of lattice elasticity from low entropy metals to medium and high entropy alloys, *Scripta Mater.* 101 (2015) 32–35.
- [2] J.Y. Wang, H.L. Yang, H. Huang, J.M. Ruan, S.X. Ji, In-situ Mo nanoparticles strengthened CoCrNi medium entropy alloy, *J. Alloys. Comp.* 798 (2019) 576–586.
- [3] A. Gail, E.P. George, Tensile properties of high- and medium-entropy alloys, *Intermetallics* 39 (2013) 74–78.
- [4] B. Gludovatz, A. Hohenwarter, K.V.S. Thurston, H. Bei, Z. Wu, E.P. George, R.O. Ritchie, Exceptional damage-tolerance of a medium-entropy alloy CrCoNi at cryogenic temperatures, *Nature. Commun.* 7 (2016) 10602.
- [5] J.Y. Wang, H.L. Yang, Z.L. Liu, S.X. Ji, R.D. Li, J.M. Ruan, A novel Fe₄₀Mn₄₀Cr₁₀Co₁₀/SiC medium-entropy nanocomposite reinforced by the nanoparticles-woven architectural structures, *J. Alloys Comp.* 772 (2019) 272–279.

- [6] T. Yang, Y.L. Zhao, Y. Tong, Z.B. Jiao, J. Wei, Multicomponent intermetallic nanoparticles and superb mechanical behaviors of complex alloys, *Science* 362 (2018) 933–937.
- [7] M. Yang, D. Yan, F. Yuan, P. Jiang, E. Ma, X. Wu, Dynamically reinforced heterogeneous grain structure prolongs ductility in a medium-entropy alloy with gigapascal yield strength, *Proc. Natl. Acad. Sci.* 115 (2018) 7224–7229.
- [8] J.P. Liu, J.X. Chen, T.W. Liu, C. Li, L.H. Dai, Superior strength-ductility CoCrNi medium-entropy alloy wire, *Scripta Mater.* 181 (2020) 19–24.
- [9] W.Y. Huo, F. Fang, H. Zhou, Z.H. Xie, J.K. Shang, J.Q. Jiang, Remarkable strength of CoCrFeNi high-entropy alloy wires at cryogenic and elevated temperatures, *Scripta Mater.* 141 (2017) 125–128.
- [10] J. Moon, J.M. Park, J.W. Bae, H.S. Do, H.S. Kim, A new strategy for designing immiscible medium-entropy alloys with excellent tensile properties, *Acta Mater.* 193 (2020) 71–82.
- [11] Z. Li, C.C. Tasan, K.G. Pradeep, D. Raabe, A TRIP-assisted dual-phase high-entropy alloy: Grain size and phase fraction effects on deformation behavior, *Acta Mater.* 131 (2017) 323–335.
- [12] Z. Li, K.G. Pradeep, Y. Deng, D. Raabe, C.C. Tasan, Metastable high-entropy dual-phase alloys overcome the strength-ductility trade-off, *Nature* 534 (2016) 227–230.
- [13] H.Y. Yu, W. Fang, R.B. Chang, X. Bai, X. Zhang, B.X. Liu, Effects of annealing temperature and cooling medium on the microstructure and mechanical properties of a novel dual phase high entropy alloy, *Mater Charact.* 163 (2020) 110291.
- [14] S. Huang, W. Li, S. Lu, F. Tian, J. Shen, E. Holmström, L. Vitos, Temperature dependent stacking fault energy of FeCrCoNiMn high entropy alloy, *Scripta. Mater.* 108 (2015) 44–47.
- [15] S. Zhao, G.M. Stocks, Y. Zhang, Stacking fault energies of face-centered cubic concentrated solid solution alloys, Stacking fault energies of face-centered cubic concentrated solid solution alloys, *Acta Mater.* 134 (2017) 334–345.
- [16] F. Otto, A. Dlouhy, C. Somsen, H. Bei, G. Eggeler, E.P. George, The influences of temperature and microstructure on the tensile properties of a CoCrFeMnNi high-entropy alloy, *Acta Mater.* 61 (15) (2013) 5743–5755.
- [17] Y. Wang, B. Liu, K. Yan, M. Wang, S. Kabra, Y.L. Chiu, D. Dye, P.D. Lee, Y. Liu, B. Cai, Probing deformation mechanisms of a FeCoCrNi high-entropy alloy at 293 and 77 K using in situ neutron diffraction, *Acta Mater.* 154 (2018) 79–89.

- [18] G. Laplanche, A. Kostka, C. Reinhart, J. Hunfeld, G. Eggeler, E.P. George, Reasons for the superior mechanical properties of medium-entropy CrCoNi compared to high-entropy CrMnFeCoNi, *Acta Mater.* 128 (2017) 292–303.
- [19] A.H.B. Gludovatz, D. Catoor, E.H. Chang, E.P. George, R.O. Ritchie, A fracture-resistant high-entropy alloy for cryogenic applications, *Science* 345 (2014) 1153–1158.
- [20] J.W. Bae, J.B. Seol, J. Moon, S.S. Sohn, M.J. Jang, H.S. Kim, Exceptional phase-transformation strengthening of ferrous medium-entropy alloys at cryogenic temperatures, *Acta Mater.* 161 (2018) 388–399.
- [21] J.Y. He, H. Wang, H.L. Huang, X.D. Xu, M.W. Chen, Y. Wu, A precipitation-hardened high-entropy alloy with outstanding tensile properties, *Acta Mater.* 102 (2016) 187–196.
- [22] H.L. Huang, Y. Wu, J.Y. He, H. Wang, X.J. Liu, Phase-Transformation Ductilization of Brittle High-Entropy Alloys via Metastability Engineering, *Adv. Mater.* 29 (2017) 1701678.
- [23] Z.W. Wang, I. Baker, W. Guo, J.D. Poplawsky, The effect of carbon on the microstructures, mechanical properties, and deformation mechanisms of thermo-mechanically treated Fe_{40.4}Ni_{11.3}Mn_{34.8}Al_{7.5}Cr₆ high entropy alloys, *Acta Mater.* 126 (2017) 346–360.
- [24] I. Baker, F.L. Meng, M. Wu, A. Brandenburg, Recrystallization of a novel two-phase FeNiMnAlCr high entropy alloy, *J. Alloy Compd.* 656 (2016) 458–464.
- [25] X.L. Wu, Y.T. Zhu, Y.G. Wei, Q. Wei, Strong Strain Hardening in Nanocrystalline Nickel, *Phys. Rev. Lett.* 103 (2009) 205504.
- [26] V. Yamakov, D. Wolf, S.R. Phillpot, A.K. Mukherjee, H. Gleiter, Deformation-mechanism map for nanocrystalline metals by molecular-dynamics simulation, *Nat. Mater.* 1 (2002) 45–48.
- [27] L. Dupuy, M.C. Fivel, A study of dislocation junctions in FCC metals by an orientation dependent line tension model, *Acta Mater.* 50 (2002) 4873–4885.
- [28] Y.L. Zhang, J.G. Li, X.G. Wang, Y.P. Lu, Y.Z. Zhou, The interaction and migration of deformation twin in an eutectic high-entropy alloy AlCoCrFeNi_{2.1}, *J. Mater Sci Technol.* 35 (2019) 902-906.
- [29] I.V. Kireeva, Y.I. Chumlyakov, A.V. Vyrodoва, Z.V. Pobedennaya, I.Karaman, Effect of twinning on the orientation dependence of mechanical behaviour and fracture in single crystals of the equiatomic CoCrFeMnNi high-entropy alloy at 77K, *Mater. Sci. Eng. A* 784 (2020) 139315.
- [30] T.H. Blewitt, R.R. Coltman, J.K. Redman, Low-temperature deformation of copper single crystals, *J. Appl. Phys.* 28 (1957) 651-660.

- [31] J.W. Christian, S. Mahajan, Deformation twinning, *Prog. Mater. Sci.* 39 (1995): 1-157.
- [32] K. Lu, F.K. Yan, H.T. Wang, N.R. Tao, Strengthening austenitic steels by using nanotwinned austenitic grains, *Scripta Mater.* 66 (2012) 878–883.
- [33] M. Bönisch, Y. Wu, H. Sehitoglu, Hardening by slip-twin and twin-twin interactions in FeMnNiCoCr, *Acta Mater.* 153 (2018) 391–403.
- [34] B.B. Zhang, N.R. Tao, K. Lu, A high strength and high electrical conductivity bulk Cu-Ag alloy strengthened with nanotwins, *Scripta Mater.* 129 (2017) 39–43.
- [35] J. Wang, H. Huang, Shockley partial dislocations to twin: Another formation mechanism and generic driving force, *Appl. Phys. Lett.* 85 (24) (2004) 5983–5985.
- [36] K.S. Ming, W.J. Lu, Z.M. Li, X.F. Bi, J. Wang, Amorphous bands induced by low temperature tension in a non-equiatomic CrMnFeCoNi alloy, *Acta Mater.* 188 (2020) 354–365.
- [37] Z. Fan, S. Xue, J. Wang, K. Yu, H. Wang, X. Zhang, Unusual size dependent strengthening mechanisms of Cu/amorphous CuNb multilayers, *Acta Mater.* 120 (2016) 327–336.
- [38] B. Cheng, J.R. Trelewicz, Design of crystalline-amorphous nanolaminates using deformation mechanism maps, *Acta Mater.* 153 (2018) 314–326.

Supplemental material

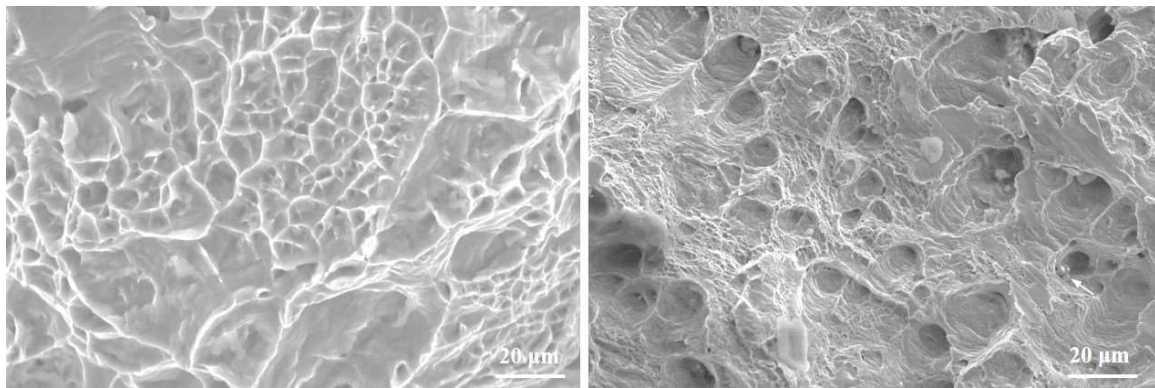


Fig. S1. The fracture surfaces of as-cast $\text{Co}_{23}\text{Cr}_{23}\text{Ni}_{23}\text{Mn}_{31}$ medium-entropy alloy tensile samples, showing minor Cr oxide nanoparticles.